Volume 18, Number 3, 2025. pp. 389-398

Jordan Journal of Physics

ARTICLE

Ultraviolet Photodetectors Based on Nanostructured SnO_2 Thin Films/P-Si Heterojunctions Prepared by a Hydrothermal Method

Abd alhameed A. Hameed[a], **J. F. Mohammad**[b] and **Isam M. Ibrahim**[c]

[a] *Ministry of Education, Education Direction in Al-Anbar, Iraq.*
[b] *Physics Department, College of Education for Pure Sciences, University of Anbar, Iraq.*
[c] *Department of Physics, College of Science, University of Baghdad, Baghdad, Iraq.*

Doi: **https://doi.org/10.47011/18.3.11**
Received on: 31/03/2024; *Accepted on: 26/06/2024*

Abstract: The aim of this work is to investigate the possibility of using SnO_2 thin films as ultraviolet (UV) detectors. Films were grown on seed layer substrates of glass and p-type Si through the hydrothermal method at different pH values (3, 9, and 11). X-ray diffraction (XRD) pattern reveals that the films are polycrystalline with a tetragonal structure, and the structure has maximum intensity in the (110) direction. The crystallite size of the prepared samples was found to vary from 5.3 to 7.3 nm. FESEM indicated that the synthesized nanoparticles also underwent morphological transformations, changing from spherical to nanorod-like like structures depending on the pH value. Energy-dispersive X-ray spectroscopy (EDS) analysis revealed that there were no foreign particles or impurities in the films. Increasing the pH from 3 to 9 changed the characteristics of the synthesized films and led to a decrease in the optical band gap from 3.3 to 3.1 eV, along with reduced optical transmittance. Current-voltage (I-V) characteristics were found to exhibit Schottky-like characteristics where photocurrent increased exponentially with the increase of the bias voltage and light intensity. The photodetector response at the extraction wavelength of 370 nm displayed a reasonable level of sensitivity, reaching up to 42.77% for the sample prepared at pH 9. All films demonstrated rise and fall times of less than one second, confirming their suitability for high-speed UV detection.

Keywords: Photo sensor, Detector, Sensitivity, Seed layer, SnO_2.

1. Introduction

Over the last decade, there has been a substantial amount of research dedicated to the study of metal oxide thin films. This research has been motivated by the recognition of their potential applications across several domains, including but not limited to solar cells, optoelectronic devices, liquid crystal displays, heat mirrors, and gas sensors. The optical transparency of undoped and doped nonstoichiometric metal oxide thin films is significant in the visible spectrum, and their conductivity closely resembles that of metallic materials [1, 2]. The technical uses of semiconductor nanocrystals are of great interest and focus. The electrical, optical, and magnetic characteristics of these particles are greatly influenced by their size [3, 4]. Numerous studies have demonstrated that altering the pH value leads to changes in the shape and size of nanoparticles, which in turn enhances the applications of metal oxides in sensors and other fields [5, 6]. Recently, considerable effort has been devoted to the systematic improvement of semiconductor oxides with unique structures or

Corresponding Author: Abd alhameed A. Hameed **Email**: abd21u3009@uoanbar.edu.iq

morphologies [7-9]. Tin dioxide (SnO_2) is a Nano scale material that includes semiconductor materials. SnO_2 is commonly used as an essential material in the fabrication of solar cells [10], transparent conductive oxides (TCOs) [11], gas sensing devices [12], and photocatalysts [13]. SnO_2 has several advantages, including high transparency and high sensitivity to gas [14]. SnO_2 thin films typically exhibit n-type semiconductor behavior, characterized by a broad energy band gap, and are commonly found in a tetragonal rutile structure [15]. Each preparation method has its drawbacks, such as the requirement of a vacuum environment, complex procedures, or high temperatures, which can lead to reduced crystallinity, contaminants, or inadequate dispersion. The hydrothermal technique, a synthetic method that involves the bottom-up approach, has gained significant popularity as a preferred approach for the synthesis of nanomaterials. This is mostly due to its straightforward procedure, ability to produce high-quality crystals, convenient control over shape, efficient sintering activity, and low temperature requirements [16, 17]. In this work, nanostructured SnO_2 thin films with varying pH values were synthesized using a hydrothermal technique. The crystal structure, morphology, and photodetector characteristics were studied.

2. Experimental Methods

Tin dioxide thin films were fabricated using a hydrothermal technique on a seeded layer. First, the glass slides were thoroughly cleaned using distilled water and ethanol in an ultrasonic bath for ten minutes. The 0.01 M tin chloride solution was then agitated on a magnetic stirrer for 30 minutes to create the precursors, which served as the sources of tin ions. The p-type silicon wafer substrate was cleaned using a solution of hydrofluoric acid (HF) and ethanol (99%) in a 1:1 ratio. Tin chloride solution was sprayed on glass and silicon (p-type) substrates using chemical spray pyrolysis at 400°C. The spraying time was 5 seconds, followed by a stop time of 20 seconds. The growth solution was created by dissolving 0.1 M tin chloride, which acts as a tin ion source, in a mixture of 70% ethanol and deionized water in a 1:1 ratio. Furthermore, 0.1 M trisodium citrate ($Na_3C_6H_5O_7$) was dissolved in deionized water and agitated for 30 minutes. Next, the two solutions were combined and agitated for 30 minutes, with varying pH levels (3, 9, and 11) achieved by introducing NaOH. These solutions were then labeled S1, S2, and S3, respectively. The ultimate blend was moved to a stainless-steel autoclave coated with Teflon, where the substrates containing seeded layers were positioned vertically inside the Teflon container. In a digitally controlled oven, the autoclave was promptly sealed and maintained at a consistent temperature of 100°C for a duration of 6 hours. Following this, the autoclave was subjected to a process of natural cooling until it attained the ambient temperature. In order to remove any residual solid particles or unreacted atoms from the surface, the substrates underwent a rinsing process using deionized water. Following that, the samples underwent a drying process in an oven set at a temperature of 100°C for a duration of 30 minutes. The annealing process took place in a furnace over a period of 1 hour at a temperature of 400°C. After that, the films were prepared for characterization.

3. Results and Discussion

3.1 Structure and Morphological Properties

Figure 1 displays the X-ray diffraction (XRD) patterns of tin dioxide films synthesized using a hydrothermal method on glass substrates at different pH values. The films exhibited a polycrystalline tetragonal structure with a preferred orientation along the (110) plane, corresponding to a diffraction angle of 26.74°. Additional diffraction peaks were observed at approximately 34° and 51.9°, corresponding to the (101) and (211) planes, respectively. These observations are consistent with standard data (JCPDS card No. 00-001-0657) and agree with previously reported results [18, 19]. The Debye–Scherrer equation, $D = k\lambda/\beta\cos\theta$, is used for the calculation of crystal size. In this equation, k denotes the shape factor (0.94), β represents the full width at half-maximum (FWHM), θ is the angle of the diffraction peak, and λ=0.15405 nm is the wavelength of the X-ray source. The crystallite size was found to be in the range of 7.26 to 7.3 nm. The average crystal size decreased when the pH increased from 3 to 9, as shown in Table 1. The pH level regulates the degree of supersaturation by altering the ionic equilibrium, particularly through changes in hydroxide ion concentration. This, in turn, modifies the interaction with tin ions, thereby controlling the nucleation process and ultimately affecting the size and morphology of the crystallites [20]. Since supersaturation acts as a

driving force for nucleation and crystal growth [21], its regulation is crucial for tailoring nanostructures. At pH 11, however, the crystallite size increased again to 7.3 nm, which is consistent with the findings of other researchers [18, 22].

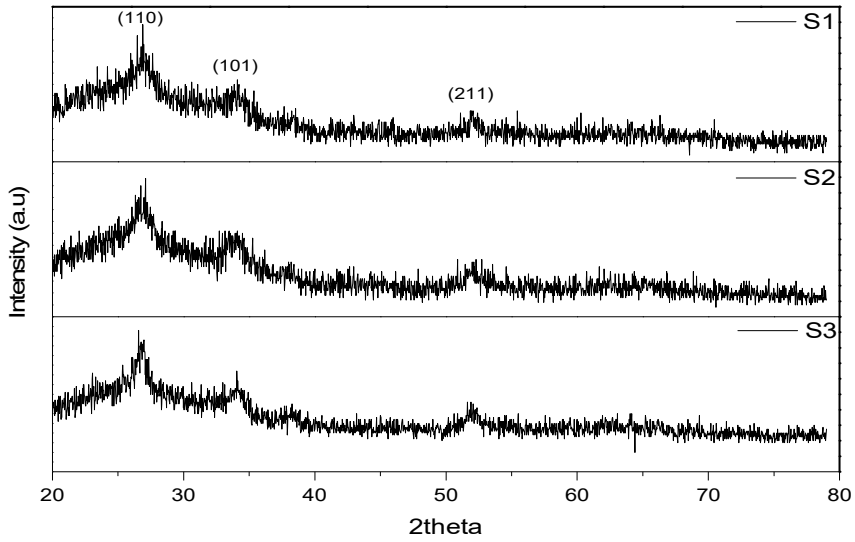

FIG. 1. XRD patterns of SnO_2: S1 (pH= 3), S2 (pH= 9), and S3 (pH= 11).

TABLE 1. Structure parameters of the prepared SnO_2 thin films at different pH values.

Sample	2θ (Exp.)	d_{hkl} Exp.(A)	d_{hkl} Std.(A)	FWHM	D (nm)	hkl	$D_{ave.}$ (nm)	System	Card No.
S1	26.74	3.21233	3.34000	1.8750	4.55	110	7.26	Tetrag-onal	00-001-0657
	34.06	2.55684	2.64000	1.1400	7.62	101			
	51.99	1.72646	1.75000	0.9600	9.62	211			
S2	26.74	3.20638	3.34000	1.8900	4.52	110	5.3	Tetrag-onal	00-001-0657
	33.94	2.56534	2.64000	1.4400	6.03	101			
	51.89	1.72963	1.75000	0.8100	5.34	211			
S3	26.74	3.21261	3.34000	1.4200	6.01	110	7.3	Tetrag-onal	00-001-0657
	34.09	2.55473	2.64000	1.2000	7.24	101			
	51.9	1.72827	1.75000	1.0800	8.55	211			

Figure 2 displays the field emission scanning electron microscopy (FESEM) images of tin dioxide samples prepared by the hydrothermal method at pH values of 3, 9, and 11 at a temperature of 100°C on glass substrates. The size and structure of SnO_2 nanoparticles were greatly affected by the pH of the reaction mixture, and the growth of nanoparticles depended on the pH of the solution. A variety of agglomerated particle shapes was discovered. At pH 3, the particles were spherical, with a size of 11.1 nm. Increasing the pH to 9 led to an increase in the particle size to 17.13 nm, and the shape changed to oval. Increasing the pH to 11 led to an increase in the particle size to 23.16 nm, and the particle shape became similar to that of nanorods or clustered worms. It is clear from above that changing the pH levels can inhibit agglomeration between molecules and lead to shape transformation [21].

The cross-sectional FESEM image is shown in Fig. 3. It is observed that the thickness of SnO_2 films is around 405.6 nm, calculated as follows:

Thickness = (422.8 + 429.5 + 364.5) / 3 = 405.6 nm

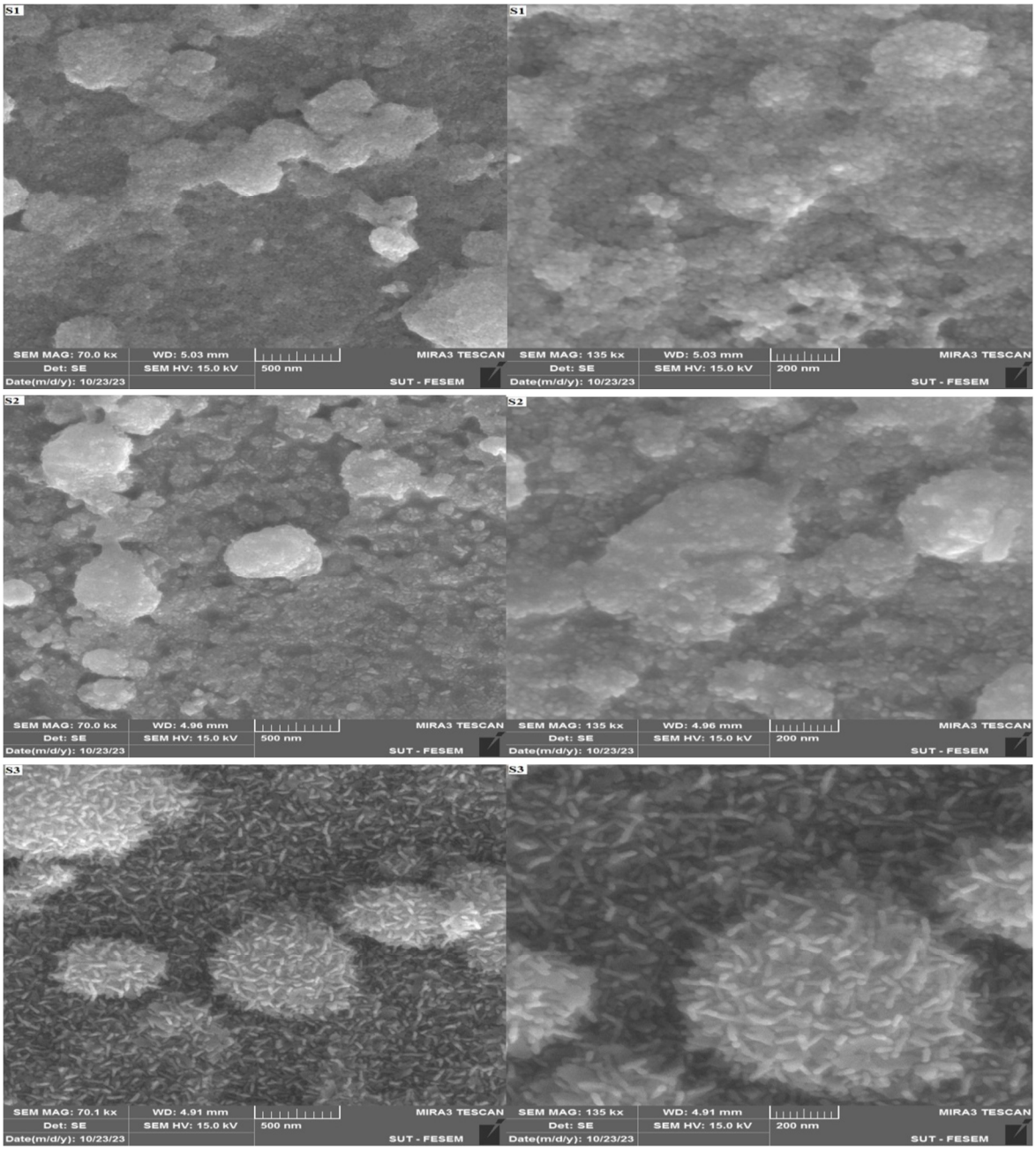

FIG. 2. FESEM images of tin dioxide thin films prepared from solutions S1 (pH = 3), S2 (pH = 9), and S3 (pH = 11).

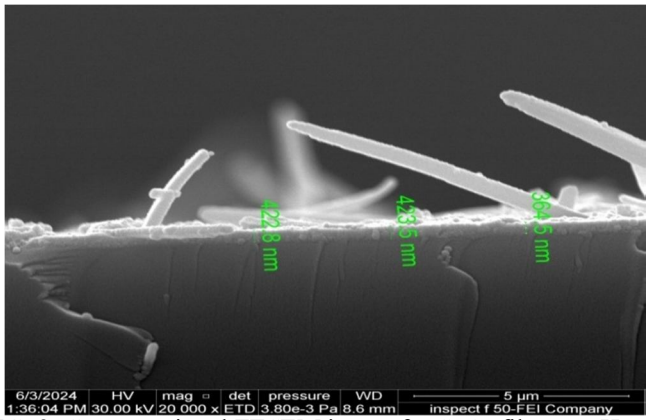

FIG. 3. Cross-sectional FESEM image for SnO_2 films at pH = 3.

Energy dispersive spectroscopy (EDS) analysis of the tin dioxide samples (S1, S2, and S3) indicated the presence of both tin and oxygen. Figures 4, 5, and 6 demonstrate that all samples exhibit a pure SnO_2 phase. The atomic ratios of tin and oxygen in the three samples were very similar, confirming the relatively homogeneous composition of the nanoparticles. The EDS results showed a strong correlation with the XRD findings. The gold peak observed originates from the gold coating that was applied to enhance conductivity during the FESEM examination.

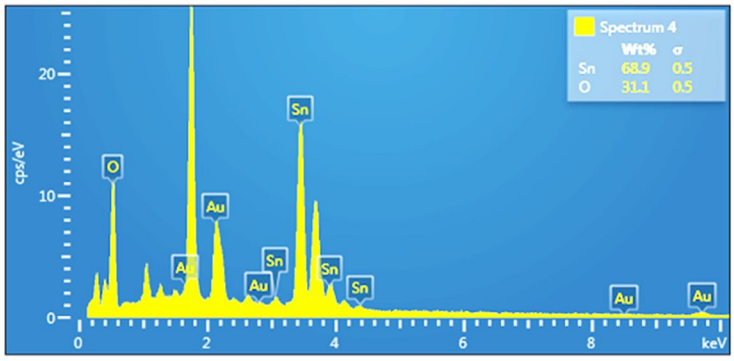

FIG. 4. EDS pattern of the tin dioxide thin film on sample S1.

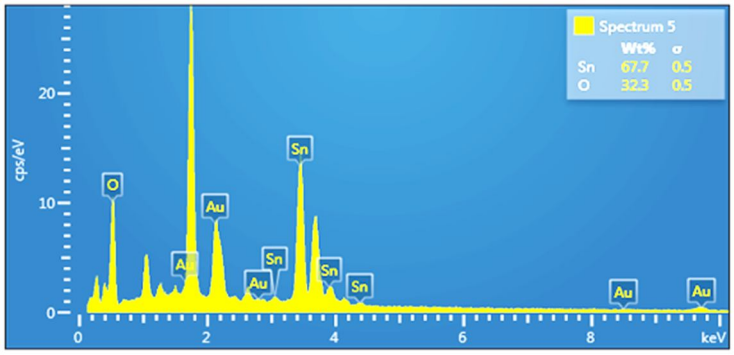

FIG. 5. EDS pattern of the tin dioxide thin film on sample S2

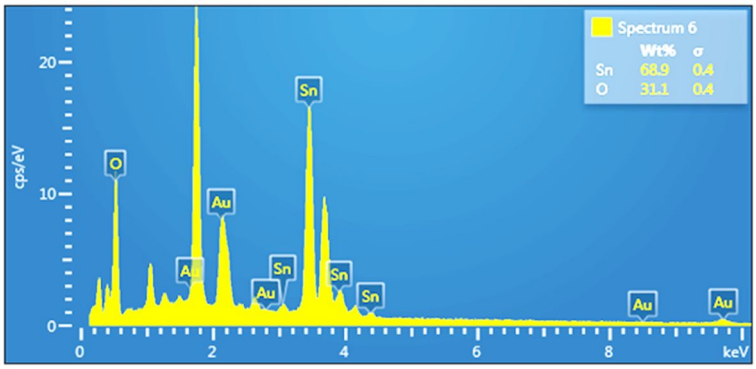

FIG. 6. EDS pattern of the tin dioxide thin film on sample S3.

3.2. Optical Properties

Optical transmittance analysis is important for various optoelectronic applications, including solar cells and photodetectors. Figure 7 displays the optical transmittance spectra of the tin dioxide thin films at pH values of 3, 9, and 11. All spectra have significant transmittance levels in the visible region, exceeding 60%. Overall, the curves exhibit good regularity, which is attributed to the uniformly distributed thickness of the film on the substrate. The decrease in transmittance is attributed to the increase in film thickness when the pH level rises. Enhanced nucleation and grain growth promoted the generation of additional Sn ions, which then reacted with oxygen ions to produce SnO_2, leading to an increase in the film thickness [19].

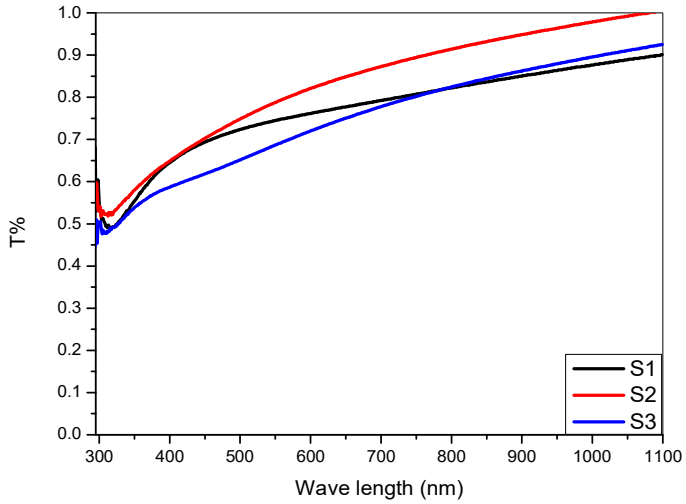

FIG. 7. Optical transmittance of SnO_2 films at varying pH values.

Figure 8 shows the optical energy gap of tin dioxide films, which was computed by extending the curve between (hv) and $(\alpha h\nu)^2$ using the following relation:

$$\propto h\nu = A(h\nu - E_g)^{1/2} \quad (1)$$

where $\propto$ represents the absorption coefficient, and A is a constant. The optical band gap values of S1, S2, and S3 were determined from the Tauc formula to be 3.3, 3.35, and 3.15 eV, respectively. These values align with the findings documented by other studies [23, 24]. The samples exhibit a reduced optical energy gap compared to tin dioxide [22, 25]. The reduced energy gap significantly contributed to the improved photocatalytic efficiency of these samples. Low-bandgap materials can absorb photons of higher wavelengths, including visible light, making them suitable as visible light-responsive photocatalysts [26].

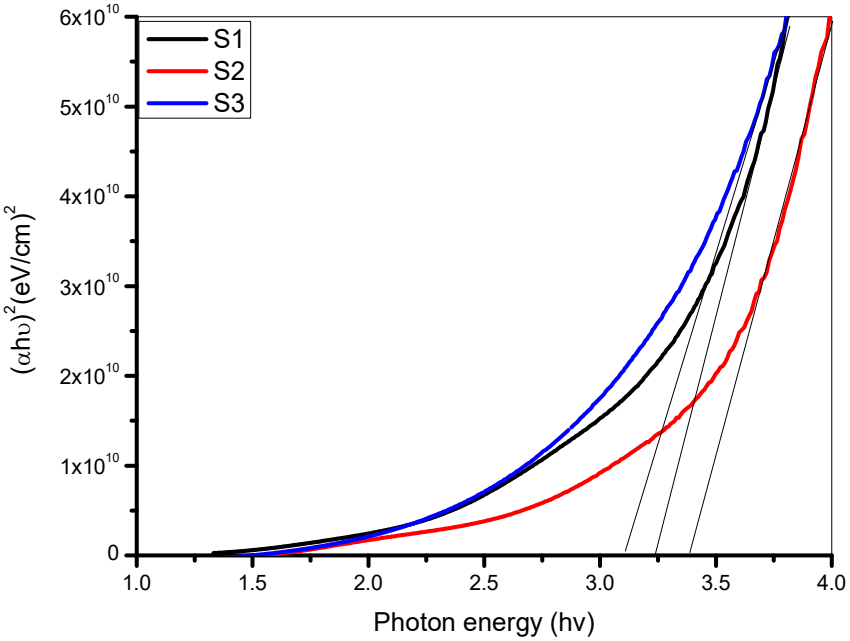

FIG. 8. Optical energy gap of SnO_2 films at varying pH values.

3.3. Current-Voltage Characteristics

The current-voltage (I-V) behavior is a crucial aspect of several interferometry techniques. Under the influence of a DC voltage sweep ranging from +1 to -1 V, the current-voltage characteristics of tin dioxide films prepared on p-Si substrates with varying pH levels (3, 9, and 11) were measured under both illuminated and dark conditions. A halogen lamp (Philips) with an intensity of 104.986 mW/cm² positioned 30 cm away from the film surface was used. The Keithley 2450 measurement unit was employed to measure the current and voltage difference, with inputs and outputs

connected via aluminum electrodes deposited on the top of a film surface. Figure 9 illustrates the current-voltage characteristics under dark conditions. Two types of currents were identified: the forward dark current, driven by majority carriers, and the recombination current occurring in the low voltage region due to the concentration of both majority and minority carriers, which exceeds the intrinsic carrier concentration. Additionally, a slight increase in the recombination current was observed for sample S3 in the low voltage region, attributed to the excitation of electrons from the valence band to the conduction band. With increasing voltage, diffusion current dominated, resulting in an exponential increase in the current. The symmetrical and nearly linear I-V characteristics indicate that the contacts for samples S1 and S2 are ohmic or semi-ohmic [27]. This behavior can be attributed to the diffusion of aluminum into the nanostructure of the oxide, creating an easier path for electron flow instead of passing through the nanostructure.

Figure 10 presents the current-voltage characteristics under illumination. The films exhibit Schottky behavior of the junction in all the manufactured devices. These graphs demonstrate that as the forward bias voltage increased, the current also increased. Increasing the reverse bias voltage widened the depletion region, leading to the separation of electron-hole pairs and an increase in current. Incidental photons of light generated a photocurrent. The number of photogenerated charge carriers in the depletion and diffusion carrier zones increased as a consequence [28, 29]. The small increase in current under illumination confirms that the device generates charge carriers in response to light, albeit in small amounts.

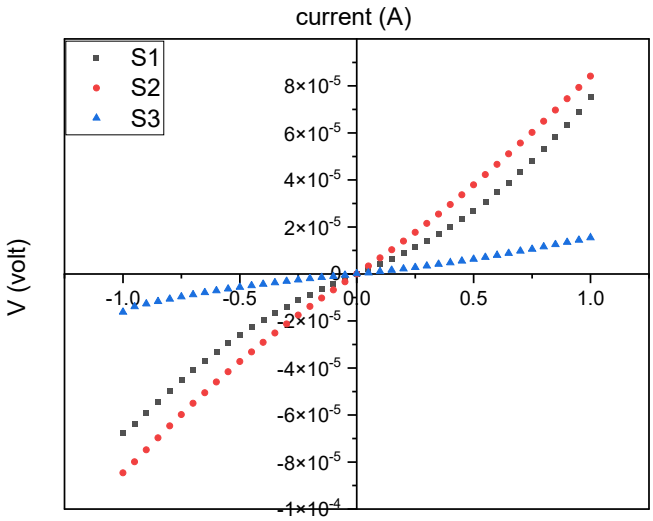

FIG. 9. I-V characteristics of SnO_2/Si-p-type materials in the dark at different pH values.

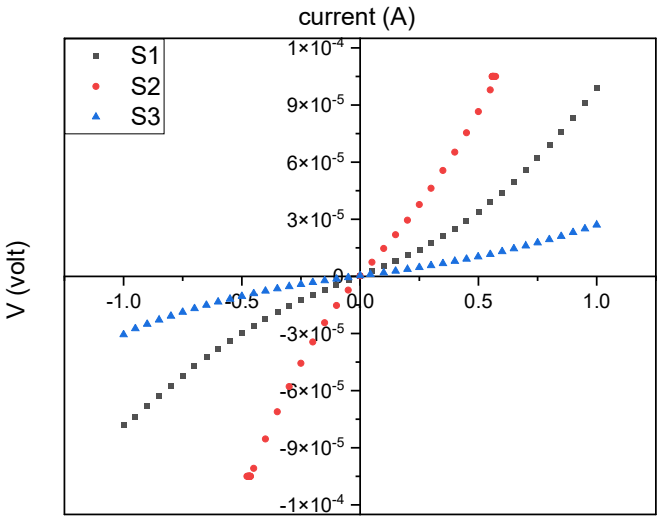

FIG. 10. I-V characteristics of the SnO_2/Si-p alloy at different pH under illumination (104.986 mW/cm^2).

3.4. Responsivity (R_λ)

The spectrum responsivity, denoted as R_λ, is a metric used to evaluate the efficiency of a system by quantifying the photocurrent produced per unit of power of the incident light intensity on the effective regions. In a photoconductive detector, the magnitude of the generated electrical signal is directly correlated with the intensity of the input light, which was approximately 0.0004 W/cm² at a wavelength of 370 nm. The determination of the spectrum responsivity of the tested detector involves calculating the ratio of the photocurrent density generated by the detector to the calculated power density, as represented by the following equation [30]:

$$R_\lambda = J_{ph}(\lambda) / P_{in}(\lambda). \quad (2)$$

Here, J_{ph} (λ) represents the density of the measured photocurrent emitted by the tested detector, whereas Pin (λ) denotes the magnitude of the incident power measurement obtained from the photoconductive detectors. Table 2 displays the spectral response values of the prepared samples, indicating that sample S2 exhibited the highest response. It is noted that this sample possesses the smallest crystallite size, as evidenced by X-ray analysis. According to the principle of quantum confinement, this suggests a heightened reactivity with the surface when exposed to light. Furthermore, the optical energy gap for this sample is approximately 3.35 eV, which aligns well with the wavelength of the ultraviolet radiation utilized.

3.5. Photosensitivity

The current-time characteristics of the prepared films were measured under irradiation in the ultraviolet region at a wavelength of 370 nm and an intensity of 0.0004 W/cm². The exposure of the thin film to light resulted in the formation of electron-hole pairs, hence causing an augmentation in the current. Once the light was turned off, the current reverted to its initial magnitude. Figure 11 shows the current-time characteristics of the films prepared on p-type silicon substrates. Figure 11 and Table 2 show that the photodetector sensitivity was approximately 2.48% for sample S1, approximately 42.77% for sample S2, and approximately 22.22% for sample S3. Additionally, the rise and fall times for all three samples were less than one second.

TABLE 2. Photo-sensitivity and responsivity (R_λ) as a function of wavelength for SnO_2/p-Si.

Sample	S% at 370 nm	R_λ (A/W)	T_{rise} (s)	T_{fall} (s)
S1 PH(3)	2.48	1.315943253	0.758	0.688
S2 PH(9)	42.77	2.532226606	0.803	0.803
S3 PH(11)	22.22	0.242888516	0.742	0.784

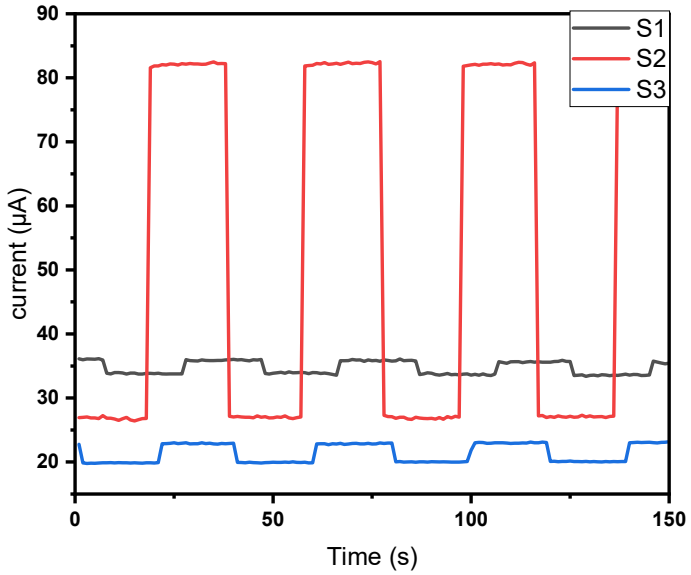

FIG. 11. Photoresponse time of SnO_2/Si-p at different pH values upon exposure to 370 nm light.

The responsivity of the devices directly depended on the photocurrent, since all three were exposed to identical optical powers. Two main factors influence the photocurrent: the

absorption of incident light and the efficient transfer of charge carriers [31]. The creation of a shallow connection between SnO_2 and p-Si facilitated the reduction in carrier distance. Additionally, the heightened prevalence of defect states, specifically vacancies and voids inside nanostructures, disrupted the mobility of photogenerated charges, thereby negatively impacting the effective conduction cross section. In addition, surface states possess the ability to ensnare carriers and generate sites for recombination [32]. Consequently, there was a notable decrease in the conduction and accumulation of carriers. Hence, the decline in the sensitivity of SnO_2/p-Si in samples S1 and S3 can be ascribed to the diminished quantity of photogenerated carriers, caused by ineffective charge transfer arising from uneven growth and the formation of shallow junctions, as well as reduced conduction area due to the heightened presence of defect states. The superior performance of S2 over the other samples was clear. Thus, the architecture of S2 can be considered highly suitable for UV detection. Further research is required to fully evaluate the effectiveness of devices employing SnO_2.

Conclusion

The hydrothermal technique was used to successfully synthesize nanostructured SnO2 thin films on the seed layer. XRD measurements showed that the crystal size could be controlled by adjusting the pH. FESEM images revealed that the particle morphology varied with pH. The optical transmittance of the SnO_2 thin films at pH 3, 9, and 11 exceeded 60% in the visible region. The optical energy gaps of S1, S2, and S3 were found to be 3.3, 3.35, and 3.15 eV, respectively. The best sensitivity and responsivity of the SnO_2/p-Si photodetector were obtained for the sample prepared at pH = 9. All prepared samples showed rise and fall times of less than one second.

Acknowledgment

This research is funded by the Scientific Committee at the Department of Physics, College of Education for Pure Sciences, University of Anbar, and the Department of Physics, College of Science, University of Baghdad.

References

[1] Guneri, E. *et al.*, Optoelectron. Adv. Mater. Rapid Commun., 3 (4) (2009) 383.

[2] Du Ahn, B. *et al*., J. Cryst. Growth, 309 (2) (2007) 128.

[3] Bargougui, R. *et al*., Adv. Mater. Lett., 6 (9) (2015) 816.

[4] Ara, M.M. *et al*., Optik, 123 (22) (2012) 2090.

[5] López-Ortiz, S. *et al*., J. Nanomater., 2020 (2020) 1.

[6] Mamakhel, A. *et al*., J. Supercrit. Fluids, 166 (2020) 105029.

[7] Gupta, V.K., Sadeghi, R., and Karimi, F., Sens. Actuators B Chem., 186 (2013) 603.

[8] Van Dang, T. *et al*., ACS Appl. Mater. Interfaces, 8 (7) (2016) 4828.

[9] Liu, J. *et al*., Sens. Actuators B Chem., 245 (2017) 551.

[10] Bittau, F. *et al*., Thin Solid Films, 633 (2017) 92.

[11] Kim, A. *et al*., Adv. Funct. Mater., 24 (17) (2014) 2462.

[12] Barsan, N., Rebholz, J., and Weimar, U., Sens. Actuators B Chem., 207 (2015) 455.

[13] Joshi, B.N., Yoon, H., and Yoon, S.S., J. Electrostat., 71 (1) (2013) 48.

[14] Susilawati *et al.* J. Phys.: Conf. Ser., 1572 (2020) 012085.

[15] Doyan, A. *et al.*, IOP Conf. Ser. Mater. Sci. Eng., 196 (2017) 012004.

[16] Zhao, J. *et al*., Appl. Sci., 13 (4) (2023) 2048.

[17] Chen, L.-Y. *et al.*, J. Nanosci. Nanotechnol., 12 (9) (2012) 6921.

[18] Van Tuan, P., Tuong, H.B., and Khiem, T.N., Commun. Phys., 31 (4) (2021) 361.

[19] Azzahra, I. *et al*., E3S Web Conf., 517 (2024) 10004.

[20] Kohli, N., Singh, O., and Singh, R.C., Sens. Actuators B Chem., 158 (1) (2011) 259.

[21] Habte, A.G., Hone, F.G., and Dejene, F.B., Phys. B Condens. Matter, 580 (2020) 411832.

[22] Mohammad, J., Sooud, M., and Abed, S., J. Ovoni. Res., 16 (2020) 107.

[23] Kumkale, V.Y. *et al.*, ES Energy Environ., 23 (2024) 1104.

[24] Chand, P., Optik, 181 (2019) 768.

[25] Kamble, V.B. and Umarji, A.M., AIP Adv., 3 (8) (2013) 082120.

[26] Zhang, H. *et al.*, Catalysts, 13 (4) (2023) 728.

[27] Çorlu, T. and Acar, S., Gazi Müh. Bilim. Derg., 9 (1) (2023) 93.

[28] Mishra, S.K. *et al.*, Opto-Electron. Rev., 18 (4) (2010) 467.

[29] Hathal, Y.R., Ibrahim, I.M., and Khalaf, M.K., Iraqi J. Appl. Phys., 20 (2B) (2024) 349.

[30] Hamdan, S. and Ali, I., Dig. J. Nanomater. Biostruct., (DJNB), 13 (3) (2018) 669.

[31] Ozel, K. *et al.*, J. Alloys Compd., 849 (2020) 156628.

[32] Mishra, M. *et al.*, ACS Omega, 3 (2) (2018) 2304.